GENERATION OF LOSSLESS DWTS FOR SPECTRAL FEATURE EXTRACTION USING DISCRETE WAVELET 2D-CNN MODEL FOR CLASSIFICATION OF HYPER SPECTRAL IMAGES

SARITHA HEPSIBHA PILLI[1], VALLI KUMARI VATSAVAYI[2]

[1,2]Department of Computer Science and Systems Engineering, Andhra University College of Engineering,

Visakhapatnam, India

E-mail: [1]sarithahepsibha@gmail.com, [2]vallikumari@gmail.com

ORCID iDs: [1]https://orcid.org/0000-0002-4756-2751, [2]https://orcid.org/0000-0002-7252-8301

ABSTRACT

In hyper spectral imaging (HSI), sensors capture detailed spectral data across numerous narrow spectral bands, resulting in high dimensionality. This dimensionality issue significantly affects HSI classification. Therefore, feature extraction (FE) for dimensionality reduction is crucial in HSI processing. This study explores the use of a 2D-Convolutional Neural Network (CNN) for HSI data analysis. Traditional 2D-CNNs, however, may not effectively integrate spectral and spatial features for HSI classification. To enhance the CNN's architecture for HSI categorization and analysis, this research investigates the integration of a lifting-scheme-based Discrete Wavelet Transform (DWT) with 2D-CNN, which we refer to as the Discrete Wavelet 2D-CNN model. The proposed methodology's main objective is to provide guidance for future research in selecting the appropriate mother wavelets for spectral FE in conjunction with a 2D-CNN classifier. By integrating 2D-CNN with the DWT, which maintains spectral signature distinctions, it may enhance the emphasis on spectral features. The novelty of this work lies in its accuracy evaluation of three DWTs: Haar, Daubechies 4-tap orthogonal filter (D4), and Cohen-Daubechies-Feauveau 9/7-tap biorthogonal filter (CDF-9/7-wavelet), for spectral FE in HSI classification using Discrete Wavelet 2D-CNN. This approach utilizes a lifting scheme-based DWT for spectral FE in HSI. The lifting-scheme is an effective nonlinear transformation approach for DWTs. The resulting spectral characteristics from wavelet decomposition are then fused with a 2D-CNN, preserving spatial information, thus creating a spectral-spatial feature vector for classification. The Discrete Wavelet 2D-CNN model's accuracy was assessed on benchmark HSI datasets, including Indian Pines (IP), Salinas (SA), and Pavia University (PU). It was observed that the D4 wavelet-based model outperformed other configurations. Furthermore, we compared the model's classification accuracy with several state-of-the-art deep learning algorithms and found that the choice of the mother wavelet for HSI spectral FE can significantly impact the model's overall performance.

Keywords: *Hyper Spectral Images (HSIs) Classification, Discrete Wavelet Transforms (DWTs), Convolutional Neural Network (CNN), Lifting-Scheme, Feature Extraction (FE)*

1. INTRODUCTION

1.1. HSI Background

Hyper spectral imaging (HSI) is the process of gathering imagery in a lot of adjacent spectral bands such that each pixel's radiant spectrum may be determined. In HSI each spectral band corresponds to a separate region of the visible-infrared spectrum [1]. Due to its fine spectral resolution with hundreds of wavelengths, HSI can capture and distinguish various earth surface objects like water, grass land, plain land and different vegetation etc. Because of the unique ability to identify different spectral reflectance values, numerous studies concentrate on utilization of HSI data in various application areas like agricultural and forest management, geology and mineralogy, invasive species detection, coastal/ocean monitoring, carbon monitoring, volcanic activity and many more [2].

1.2. Challenges In HSI Classifications

Although HSI data can discriminate among different target objects on earth with comparable surface properties, the narrow and contiguous spectral bands produce redundant information. This redundancy is unnecessary and compromises the goal of collecting HSI data.

In recent years, wide ranges of processing methods that can effectively extract data from remotely sensed HSI cubes have been developed. Specifically, feature extraction (FE) and feature selection (FS) are the two techniques that help reduce the HSI dimensionality. By using the FE approach, the initial feature space is transformed into a new feature space, whereas the FS technique selects a small number of important characteristics while eliminating unnecessary, redundant, or noisy features. Researchers have recently concentrated on a number of metaheuristic techniques that are frequently employed to look for an ideal or nearly ideal subset of characteristics in HSI. For instance, authors of [3] have developed a metaheuristic optimization strategy for FS in HSI classifications. Further, there have been numerous variations of works done that use HSI classification along with FE approaches to enhance the efficiency of classification algorithms [1, 4, and 5].

Although the two methods—FE and FS—help to reduce the HSI data's dimensionality, the primary goal of our research is to assess the efficiency and performance of wavelet-based FE methods with regard to HSI classification.

1.2.1. Spectral-spatial FE methods

There are numerous spectral-spatial feature mining techniques for the classification of HSI in the literature. For instance, simple linear iterative clustering (SLIC), gabor filter, extended morphological profiles (EMPs) and the multiple kernel learning have been proposed as spectral and spatial feature based classification frameworks of HSI [6-9]. Researchers in [10] have investigated spatial consistency by dividing HSIs into several super pixels based on their similarity in terms of intensity or textures. These spectral-spatial characteristics and hyper-parameters, however, are task-specific and selected in accordance with the data at hand. Performance in classification is influenced by the volume of training samples [11]. Additionally, majority of spectral-spatial HSI classification algorithms might not be able to distinguish small differences between classes or significant differences within classes. Therefore, one of the main problems with HSI categorization still involves the process of obtaining more discriminative features.

Recent studies have suggested incorporating Wavelet Transform (WT) into FE system for HSI classification task. Wavelet filters for dimensionality reduction allow for the separation of classes without severely losing the original data. It has been found that Discrete Wavelet Transforms (DWTs), a subset of WT approaches, significantly improve the performance of FE [12]. The authors of [13] looked towards lowering the dimensionality of HSI using a variety of wavelet filters. The authors in [14] proposed a reliable classification method based on 3D-DWT for HSI classification by taking into account DWTs' capacity for extracting the spatial and spectral information.

Motivated by those successful applications in the literature, the method of DWT is chosen for analysis in this work among the variety of already existing techniques for HSI-FE. Different wavelet families and basis functions can be used to create DWTs. It is seen in the literature, many methods are suggested for creating quick and low-power DWTs [15]. Specifically an approach called Lifting Scheme [16-19] provides less power consumption and uncomplicated design for DWTs. Instead of set of filters, it (Lifting Scheme) is based on simple predict and update mechanism for DWT implementation. Lifting scheme creates new wavelets from mother wavelets depends on the domain characteristics. Many different mother wavelets are available for DWT. The properties of the final transform are determined by the mother wavelet.

Therefore, when choosing the mother wavelet, care should be given to the specifics of a given application. In the wavelet family, Daubechies wavelets [20, 21] are the most common, and Haar wavelets are the simplest. The wavelets are chosen for the intended application based on their forms and ability to analyse the signal.

1.2.2. Deep learning-based techniques for classifying HSI

Along with the foregoing spectral-spatial FE methods for HSI, current publications also demonstrate HSI classification using various CNN models [5, 22]. A growing number of studies are examining HSI categorization methods using

FuSENet, hybrid 3D-2D CNNs, 3D CNNs and 2D-CNNs to investigate HSI categorization approaches [23, 24, 25-29]. Additionally, Residual Networks, Recurrent Neural Networks (RNNs), Double-branch Networks, Graph CNNs, Generative Adversarial Networks, and Capsule Networks are frequently employed in HSI categorization [13, 30-36]. On the other hand, in [37] it is stated that due to the limitations of HSI data, it is challenging to get acceptable spectral-spatial properties with standard convolution in independent models (such as 2D, 3D and 3D-2D CNNs).

To resolve the above-mentioned issue, researchers initiated investigations into the extraction of valuable spectral-spatial attributes employing versatile models. These models include the integration of CNN with Graph Residual Architecture [38], FPGA-Fast Patch-Free Global Learning Framework [39], SSRN-Spectral-Spatial Residual Network [40] and spectral-spatial-dependent global learning model [1]. These models can classify HSIs with a high degree of classification accuracy.

However, most existing methods are still based on convolution operations for spectral-spatial feature extraction thus exhibit high computational complexity. The literature has shown that convolution is insufficiently effective for high-resolution remote sensing pictures such as HSIs and primarily captures the spatial properties while neglecting its spectral aspects because of its linearity. In comparison to FE based on convolution, the wavelet transform is lighter, faster, and capable of nonlinear transformation [41]. Therefore, the wavelet transform might be viewed as a preferable alternative implementation for spectral FE in future CNN-based HSI scene categorization research.

1.3. Motivations And Contributions

Our present work in this paper was motivated by the successful integration of wavelet transform with 2D CNN model (SpectralNet) in [37] for extracting discriminative features of multi-resolution HSI classification. Furthermore, in [22], an approach named CNN-MHWF2N (Combining Multilevel Haar Wavelet Features with CNN Enhancement) was explored. While the previously mentioned HSI approach demonstrated superior results, it's worth noting that these models primarily emphasized the utilization of the Haar wavelet to capture spectral-spatial information.

Indeed, concerning DWT, the Haar wavelet exhibits limited utility. It excels in handling signals primarily composed of square waveforms; however, its effectiveness diminishes when confronted with the processing of broader harmonic waveforms, as it does not yield distinct information in such cases. Moreover, there exists an extensive variety of mother wavelets, and the choice of the mother wavelet can significantly impact the accuracy of 2D-CNN. Hence our paper provides further investigation of this subject with multiple discrete wavelet functions for HSIs, with the goal of providing an in-depth comparison of the methodologies. It is needed because different mother wavelets applied to the same signal might provide different outcomes, choosing the best mother wavelet for the task at hand is the key problem when utilizing wavelet transforms. In addition, motivated by the effective use of the lifting method as a superior substitute implementation for the convolution in basic CNNs in [42], our current research relies on the lifting-scheme approach to produce truly loss-less DWTs for spectral FE in Discrete Wavelet 2D-CNN model. This may be a new direction for better extraction of discriminative spectral features for HSI classification.

1.3.1. Strategy and organization

During the pre-processing phase of Discrete Wavelet 2D-CNN model, the original HSI dimensionality is decreased using the factor analysis (FA) technique. After that, patches are generated to input into the model. Then, multi-level decomposition features (spectral) are produced using lifting scheme-based discrete wavelet decomposition, and these features are combined with multi-layer convolution features (spatial) to build a spectral-spatial feature vector. Subsequently, this spectral-spatial feature vector serves as input for the dense layers within a 2D CNN.

In this study, we utilize a four-level wavelet decomposition based on the lifting scheme and implement a four-layer CNN in Python to construct the classifier under examination. We use HSI data cubes sourced from benchmark datasets, including Indian Pines (IP), Salinas (SA), and Pavia University (PU). We opted to assess the accuracy of the Discrete Wavelet 2D-CNN model with respect to the three core discrete wavelets, Haar, Daubechies 4-tap orthogonal filter (D4), and Cohen-Daubechies-Feauveau 9/7-tap biorthogonal filter (CDF-9/7-wavelet). Subsequently, we provide a comprehensive evaluation report confirming the

enhancements in HSI data classifiers achieved through the incorporation of the wavelet technique. As a result, this work focuses on presenting a summary of wavelet approaches for Spectral-Spatial FE and comparing the performance of the model with various wavelet combinations in classification of HSI.

The remainder of this document is structured as follows: Section II details the methodology for implementing the wavelet functions and the Discrete Wavelet 2D-CNN framework. Section III delves into the analysis and discussion of the classification performance of Discrete Wavelet 2D-CNN-HSI, focusing on the three fundamental discrete wavelet functions. It also includes a comparison with existing deep learning methods in terms of classification performance. Finally, the last section presents the conclusion of this work.

2. MATERIALS AND METHODS

In this section, we first consider the idea of Discrete Wavelet Transform (DWT) for FE. Then we present the Lifting Scheme for implementing DWT. With that, we provide the lifting scheme implementation for 3 basic discrete mother wavelets-- Haar, Daubechies 4-tap orthogonal filter (D4), and Cohen-Daubechies-Feauveau 9/7-tap bi-orthogonal filter (CDF-9/7-wavelet) in HSI-FE. Finally, Lifting Scheme based Discrete Wavelet 2D-CNN framework is described. This section also includes a description of the datasets utilized in the experiments.

2.1. DWT In FE

The time-frequency localization feature of the DWT has made it popular in signal and image processing. Figure 1 illustrates the DWT which is constructed through an iterative filtering process. As depicted in figure 1, at each decomposition level, the input image undergoes filtering using two filters: a Low Pass Filter (LPF) and a High Pass Filter (HPF). For each level of decomposition, the LPF produces coarse approximations, while the HPF produces detailed information of the input image. The output of this LPF is recursively filtered until the necessary depth has been reached or until no more filtering is possible.
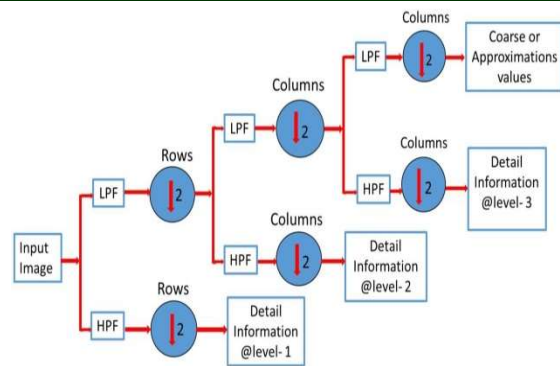

Figure 1: A 3-Level DWT Decomposition

This method, known as forward DWT, decomposes the image first row-wise and then column-wise using high pass and low pass filters.

Similar to the forward DWT, the inverse DWT (IDWT) can also be used to recover the reconstructed image. Inverse DWT uses filter banks that are referred to as synthesis filters, while forward DWT uses analysis filters [43].

2.2. Lifting Scheme For DWT

Traditional DWT involves decomposing Finite Impulse Response (FIR) filters, or filters having real coefficients, and subsampling them. In order to avoid the computational demands associated with conventional DWT methods, Wim Sweldens introduced a novel DWT design approach in 1996, referred to as the Lifting Scheme [44]. Split, Predict, and Update are the three steps of this strategy (see figure 2).
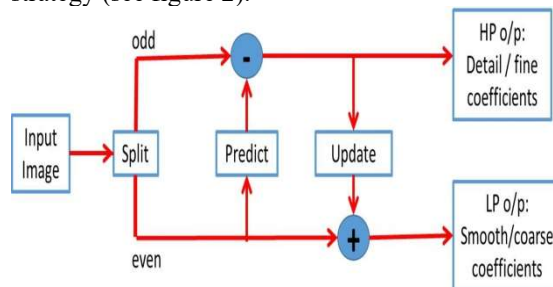

Figure 2: Forward Lifting Scheme For DWT

- **Step1-** Split: This phase takes an input signal $X = (x_k)$, where k is an integer with real samples x_k. It splits this input data into 2 separate sets such as:
  even ($X_e = x_{2k}$) and odd ($X_o = x_{2k+1}$) indexed samples.
- **Step2-** Predict: Since the correlation between the above two sets is strong. As a result, using one set, such as the even, one may create a

good predictor called P for the other set (Of course the predictor need not be exact).
So the difference or detail d_k: X_o –Predict (X_e).

- **Step3-** Update: The above prediction step can handle the spatial correlation, however for wavelets to achieve some separation in the frequency domain, the 3rd step replaces the even indexed samples with smoothened values s_k by using an Update(U) operator applied on the details, s_k: X_e + Update(d_k).

Here the update operator will be used to keep the correct running average of the even samples and reduces the aliasing (under-sampling) errors. It is because the even sample set was created through simple subsampling, its running average differs from that of the original samples.

The above steps correspond to the forward transform. The lifting scheme for Inverse DWT can be designed in a similar way. A clear representation of the implementation steps in forward and inverse transforms of lifting scheme are provided in table 1 and table 2 respectively.

Table 1: Lifting Scheme Steps In Forward Transformation Or Decomposition.

Split:	$Split(X) = \begin{cases} X_e = x_{2k} \\ X_o = x_{2k+1} \end{cases}$
Predict:	Wavelet (or) Detail Coefficients @Level-k : $d_k = X_o - Predict(X_e)$
Update:	Smooth(or)Approximate Coefficients @Level-k : $s_k = X_e + Update(d_k)$

Table 2: Lifting Scheme Steps In Inverse Transformation Or Reconstruction.

$X_e = s_k - Update(d_k)$
$X_o = d_k + Predict(X_e)$
$x_{2k} = X_e$ and $x_{2k+1} = X_o$

Unlike conventional procedures, this lifting scheme does not require complex mathematical calculations. As opposed to conventional convolution-based DWT, it requires half as many computations. From the even samples, odd samples are created, and update and prediction blocks are used in place of filters.

2.3. Basic DWTS For FE Using Lifting Scheme

In this study, each pixel of HSI patch will be individually decomposed in the spectral domain using the discrete 2D Wavelet transform. Due to the wavelet's inherent ability to retain peaks and

troughs in standard spectra, it becomes possible to extract the majority of discriminative multiscale features using the DWT. Selecting the right wavelet family is essential when employing the wavelet transform. There will be different types of wavelets available, for instance, orthogonal and bi-orthogonal. Bi-orthogonal wavelet filters produce two sets of scaling functions and wavelets: one pair for decomposition and another pair for reconstruction. In contrast, orthogonal wavelet filter banks generate a single pair for both the decomposition and reconstruction processe. In this section, we discuss some of the most basic wavelet families with implementation details using lifting scheme.

2.3.1. Haar wavelet

Alfred HAAR invented the HAAR wavelet in 1909 as a simplest and most straightforward orthogonal wavelet. It is a step-like, discontinuous function with excellent temporal localization but poor frequency localization. They can reproduce constant functions only. The HAAR wavelet transform is quick, easy on the memory, and easy to comprehend. In the Haar wavelet, the discrete signal is split into two sub-signals, with each sub-signal having half the length of the original signal.

Lifting scheme on HAAR WT:

There are two steps in the lifting scheme for HAAR WT: one Predict 'P' and one Update 'U'. The split procedure that divides input signal 'X' into even 'X_e' and odd 'X_o' samples is depicted in figure 3.

All the forward and inverse transform operations are given in equations 1–6.

Forward transformation-HAAR- WT:
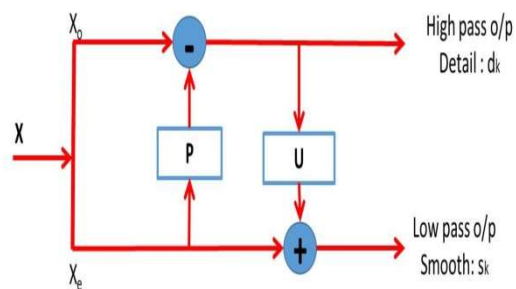$$Split(X) = \begin{cases} X_e = x_{2k} \\ X_o = x_{2k+1} \end{cases} \quad (1)$$

Figure 3:Lifting Scheme For HAAR DWT

$$Predict: d_k = X_o - X_e \qquad (2)$$

$$Update: s_k = X_e + \frac{1}{2}d_k \qquad (3)$$

Inverse transformation-HAAR- WT:

$$X_e = s_k - \frac{1}{2}d_k \qquad (4)$$

$$X_o = d_k + X_e \qquad (5)$$

$$\begin{cases} x_{2k} = X_e \\ x_{2k+1} = X_o \end{cases} \qquad (6)$$

From equations 2 & 3, it is evident that the detail (or wavelet) coefficient (d_k) in prediction step for HAAR wavelet is just the distinction between an odd (X_o) and an even (X_e) samples. Then, to restore the right running average and to resolve the under-sampling (or aliasing) issue, the HAAR wavelet's update lifting step will add half of the detail (or wavelet) coefficient to the even samples to yield the s_k value, (it is because, as stated in [44], two even locations are influenced by the approximation scale, which is twice the detail scale).

2.3.2. Daubechies 4-tap orthogonal filter (D4) wavelet

A continuous, piecewise smooth signal model is incompatible with the HAAR wavelet since it is a step function and cannot approximate an analogue signal. Thankfully, Ingrid Daubechies developed orthonormal wavelet bases in 1988, which are compatible with continuous, piecewise smooth signal models. In addition, Daubechies filters are often known as maxflat filters since their frequency response provides the greatest flatness at 0 and π. The D2 to D20 range covers the Daubechies family of orthogonal wavelets. The D2 wavelet is same as Haar wavelet. For our research, we take into account the Daubechies 4-tap orthogonal filter (D4), the most basic wavelet in the Daubechies family with two vanishing moments. The number of analysis filter coefficients is represented by the 4 tap. The vanishing moments, which are equal to half of the filter coefficients, are a need for the smoothness of the wavelet function.

Constructing and inverting the Daubechies 4-tap orthogonal filter (D4) wavelet transform is straightforward. Like the Haar transform, it can be performed through a series of decompositions. However, D4 differs in having a filter length greater than two. Consequently, it offers a more concentrated and consistent transformation.

Lifting scheme on daubechies 4-tap orthogonal filter (D4) WT:

The Lifting-scheme for D4 WT is depicted in figure 4. It has four steps, as shown in figure 4: predict1 'P₁', update1 'U₁', predict2 'P₂', normalization - 'N₁' and 'N₂'.
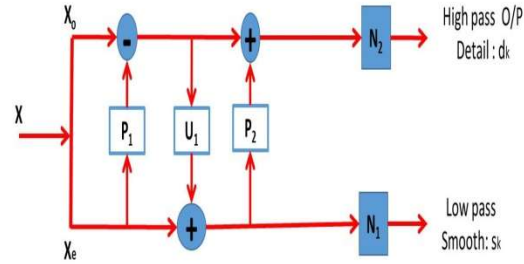

Figure 4:Lifting Scheme For D4 DWT

The lifting scheme uses less memory and doesn't need a temporary storage like regular D4. The forward operations for D4 are provided in equations 7–11. As seen in equations 12 through 16, the inverse transform results from reversing the operations and flipping the signs.

Forward transformation- D4- WT:

$$Predict\ 1: d_k^1 = X_o - \sqrt{3}X_e \qquad (7)$$

$$Update\ 1: s_k^1 = X_e + \frac{\sqrt{3}}{4}d_k^1 + \frac{(\sqrt{3}-2)}{4}d_{k+1}^1 \qquad (8)$$

$$Predict\ 2: d_k^2 = d_k^1 + s_{k-1}^1 \qquad (9)$$

$$Normalization\ 1: s_k = \frac{(\sqrt{3}+1)}{\sqrt{2}}s_k^1 \qquad (10)$$

$$Normalization\ 2: d_k = \frac{(\sqrt{3}-1)}{\sqrt{2}}d_k^2 \qquad (11)$$

Inverse transformation- D4- WT:

$$d_k^2 = \frac{(\sqrt{3}+1)}{\sqrt{2}}d_k \qquad (12)$$
$$s_k^1 = \frac{(\sqrt{3}-1)}{\sqrt{2}}s_k \qquad (13)$$

$$d_k^1 = d_k^2 - s_{k-1}^1 \qquad (14)$$

$$X_e = s_k^1 - \frac{\sqrt{3}}{4}d_k^1 - \frac{(\sqrt{3}-2)}{4}d_{k+1}^1 \qquad (15)$$
$$X_o = d_k^1 + \sqrt{3}X_e \qquad (16)$$

2.3.3. Cohen-Daubechies-Feauveau 9/7-tap bi-orthogonal filter

The term "CDF-9/7 Wavelet" is an alias for the Cohen-Daubechies-Feauveau 9/7-tap Bi-

Orthogonal Filter Wavelet. This wavelet employs a 9-coefficient analysis low-pass filter and a 7-coefficient synthesis low-pass filter. Both the analysis and synthesis high-pass filters possess four vanishing moments, and they exhibit symmetric scaling and wavelet functions. These characteristics make them particularly popular for use in picture compression applications.

Lifting scheme on CDF- 9/7- wavelet:

The five steps constituting the lifting scheme for the CDF-9/7 Wavelet are depicted in figure 5: predict1 'P$_1$', update1 'U$_1$', predict2 'P$_2$', update2 'U$_2$', normalizations – 'N$_1$' and 'N$_2$'.

The complexity and the lifting steps of CDF-9/7 wavelet are greater than those of D4 wavelet as the filter coefficients rise. Equations 17 to 23 provide the forward transform operations, while equation 24 lists the values of the constants.
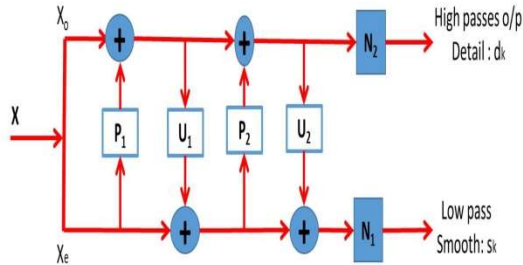

Figure 5: Lifting Scheme For CDF-9/7 DWT

Forward transformation- CDF- 9/7- WT:

$$Split(X) = \begin{cases} s_k^0 = x_{2k} \\ d_k^0 = x_{2k+1} \end{cases} \quad (17)$$

$$Predict\ 1: d_k^1 = d_k^0 + \alpha(s_k^0 + s_{k+1}^0) \quad (18)$$

$$Update\ 1: s_k^1 = s_k^0 + \beta(d_k^1 + d_{k-1}^1) \quad (19)$$

$$Predict\ 2: d_k^2 = d_k^1 + \gamma(s_k^1 + s_{k+1}^1) \quad (20)$$

$$Update\ 2: s_k^2 = s_k^1 + \delta(d_k^2 + d_{k\_1}^2) \quad (21)$$

$$Normalization\ 1: s_k = \zeta s_k^2 \quad (22)$$

$$Normalization\ 2: d_k = \frac{d_k^2}{\zeta} \quad (23)$$

And,

$$\begin{aligned} \alpha &= -1.586134342 \\ \beta &= -0.05298011854 \\ \gamma &= 0.8829110762 \\ \delta &= 0.4435068522 \\ \zeta &= 1.149604398 \end{aligned} \quad (24)$$

2.4. Discrete Wavelet 2D-CNN framework

After covering the basic specifics of the DWT methods needed in HSI - FE, we now attempt to describe the overall Discrete Wavelet 2D-CNN model used for HSI categorization in our present work. The steps of the adopted model are represented in figure 6 as follows:
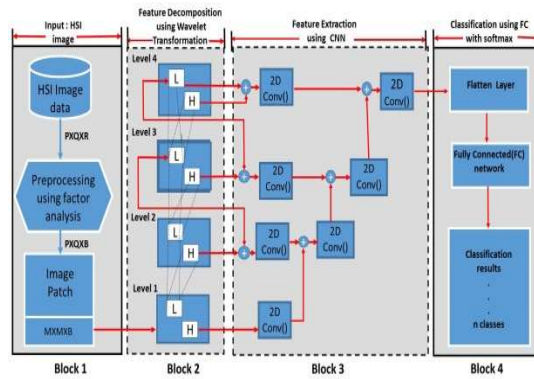

Figure 6: Outline Of The Wavelet CNN- Model For Classification Of HSI

The initial step involves working with an HSI cube with dimensions (P, Q, and R), where P and Q represent the spatial dimensions, and R corresponds to the spectral dimension. Next, to reduce the massive dimensionality of the HSI data, the model must go through pre-processing phase. Among a variety of available methods to minimize the HSI dimensionality, FA-Factor Analysis is used in the current model. Since in HSI, it is required to differentiate similar variables effectively and commonly used PCA approximates the necessary variables but is not very effective at differentiating closely related variables.

Contrarily, FA is a technique for condensing the number of variables in a dataset into a small number of factors by extracting the highest common variance from each variable and converting it to a common scale. As a result, training takes less time. Hence FA is beneficial in HSI pre-processing. By using this FA algorithm, the original HSI cubes are changed to a size (P, Q and B). Subsequently, the Wavelet 2D-CNN is employed to handle the extracted patches, which have dimensions (M, M, and B).

The discrete wavelet block is applied to obtain a four-level decomposition of spectral information for every extracted HSI patch. Next, to capture spatial characteristics, four convolution layers are employed. In this context, the spatial information from each convolutional layer is integrated with the decomposition features from each level of the wavelet transform to acquire a 2-D spectral-spatial feature vector. In contrast to a 3D CNN, the spectral characteristics obtained through DWT require fewer computational resources.

Lastly, the architecture includes an average pooling layer (used for filtering and reducing the number of outputs from the convolution layers before passing them to subsequent layers), multiple fully connected (FC) layers, and a softmax classifier, which collectively assess classification accuracies.

Within the Discrete Wavelet 2D-CNN technique, the labeled samples of each dataset are partitioned into two subsets: the training data (X_{train}) along with their corresponding labels (Y_{train}) and the testing data (X_{test}) along with their respective labels (Y_{test}). The training data is utilized for parameter updates, while the testing data is employed to evaluate the model's generalization performance.

For this project, we chose the "Categorical Cross-entropy" loss function and the "Stochastic gradient descent (SGD)" optimizer. The loss function equation is as follows:

$$L = -\sum_{i=1}^{n}(y_i * \log \hat{y}_i) \qquad (25)$$

In this equation, "n" represents the number of categories, y_i denotes the probability value for the 'iᵗʰ' class in the actual sample labels: $Y = \{y_1, y_2, ... y_n\}$, and $\hat{y}_i$ represents the probability value corresponding to the 'iᵗʰ' class in the predicted sample labels: $\hat{Y} = \{\hat{y}_1, \hat{y}_2, ... \hat{y}_n\}$.

2.4.1. Multi-level wavelet feature decomposition

To enable a hierarchical breakdown of HSI data within a multi-resolution CNN, the 2D DWT uses the following four kernels (f_{LL}, f_{LH}, f_{HL}, f_{HH}) for wavelet transform, as stated in [41]. In this study, f_{LL} is the low-pass wavelet kernel, and it is employed as the scaling function. Furthermore, f_{LH}, f_{HL} and f_{HH} serve as the high-pass wavelet kernels, being utilized as the wavelet kernel functions at each level of the hierarchical decomposition of the HSI data.

Given an input image patch f(x, y) with size MxM, the four wavelet kernels(f_{LL}, f_{LH}, f_{HL}, f_{HH}) with fixed parameters and a stride of 2, produce four sub-image features: f_{HH}(x, y), f_{HL}(x, y), f_{LH}(x, y) and f_{LL}(x, y).

Thus, mathematically we can define the DWT operation as:

$$
\begin{aligned}
f_{LL}(x,y) &= (f_{LL} * f(x,y)) \downarrow 2 \\
f_{LH}(x,y) &= (f_{LH} * f(x,y)) \downarrow 2 \\
f_{HL}(x,y) &= (f_{HL} * f(x,y)) \downarrow 2 \\
f_{HH}(x,y) &= (f_{HH} * f(x,y)) \downarrow 2
\end{aligned}
\qquad (26)
$$

In this context, equation 26 signifies the first-order wavelet decomposition. In this equation, '*' represents the convolution operator, and '↓2' denotes the standard down-sampling operation with a factor of 2. The result, f_{LL}(x, y) corresponds to the approximate sub-image, while (f_{LH}(x, y), f_{HL}(x, y), f_{HH}(x, y)) represent the detail sub-images.

This decomposition process is iteratively applied to the approximate sub-image f_{LL}(x, y), and continues until four levels of decomposition are reached. This concept is depicted in figure 7. Strong time-frequency localization of the wavelet transform enables it to translate various underlying visual features into various wavelet coefficients, enabling deeper feature extraction.
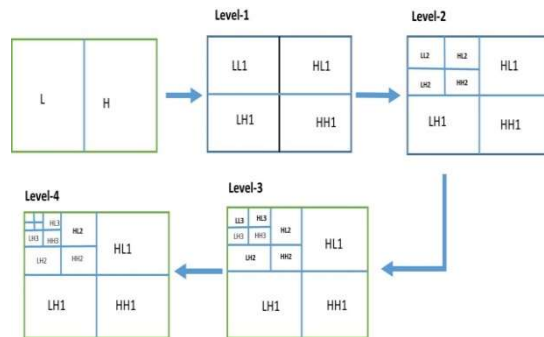

Figure 7: Feature Decomposition Using Four Levels of Wavelet Analysis [13]

In our methodology, we employ a wavelet transform to partition a HSI patch into sub-bands, and the convolutional layers are utilized to learn the spectral and spatial aspects by processing these sub-bands. The wavelet transform breaks down the sub-band component in the subsequent layer and forwards it to the convolution layer. This iterative

process is maintained in each layer of the CNN, enabling the continuous learning of spectral-spatial characteristics within HSI patches.

Specifically, for an input HSI image patch f(x, y) of size MxMxB (we take B =3 for our experiments), we can define the current Wavelet 2D-CNN model as follows:

$$F^1 = Conv + ReLU(f_1^{DWT}(x,y), K_{3*3}) \qquad (27)$$

$$F^2 = Conv + ReLU(Concate[F^1, Conv + ReLU(f_2^{DWT}(x,y), K_{3*3})], K_{3*3}) \qquad (28)$$

$$F^3 = Conv + ReLU(Concate[F^2, Conv + ReLU(f_3^{DWT}(x,y), K_{3*3})], K_{3*3}) \qquad (29)$$

$$F^4 = Conv + ReLU(Concate[F^3, Conv + ReLU(f_4^{DWT}(x,y), K_{3*3})], K_{3*3}) \qquad (30)$$

In equations 27-30, f_l^{DWT}(x, y) corresponds to 4 discrete wavelet decomposed sub band images (i.e. f_{LL_l}(x, y), f_{LH_l}(x, y), f_{HL_l}(x, y) and f_{HH_l}(x, y)), here l value reflects the level of decomposition and it takes values from 1 to 4. K represents 3x3 kernels that are utilized as convolution filters. And F^1, F^2, F^3 are the intermediate spectral-spatial features extracted during the first 3 levels and F^4 gives the final level's spectral-spatial feature map. To enhance information flow and HSI feature richness, the model provides sequential interactions among the obtained four-level features.

Then these fused features serve as input to the final stage of the developed model. This stage encompasses an average-pooling layer, two fully connected layers, and a softmax classifier, ultimately yielding the prediction results.

2.5. Materials

For evaluating the performance of our current approach, we have utilized the datasets [45], which include Indian Pines (IP), Salinas (SA), and University of Pavia (PU). These are the state-of-the-art agricultural, rural-urban and urban HSI datasets in remote sensing and image analysis. These datasets are frequently used for creating and testing algorithms and models for feature extraction, classification, and other related tasks for Hyper spectral images [4, 12, 14, 22-24, 37, 40-42].

Indian Pines (IP) Dataset

The Indian Pines (IP) data set comprises hyper spectral images of agricultural and urban areas in North-western Indiana, constituent state of the USA. The AVIRIS sensor collected this information, which includes 224 spectral reflectance bands in the wavelength range of 0.4–2.5 10^{-6} meters. By deleting bands that cover the water absorption zone, the 224 spectral bands are reduced to 200. The scene is 145 pixels wide by 145 pixels tall. This IP dataset is composed of two-thirds cropland and one-third woodland or other naturally occurring permanent vegetation. There are two major dual-lane motorways, a rail line, a few low-density homes, various man-made structures, and minor roadways. In terms of land use and land cover, the dataset has 16 classes (as indicated in table 3), with 1972 training samples and 7392 testing samples. This dataset intends to address problems with mapping land cover, detecting crop diseases, and classifying crops.

Salinas (SA) Dataset

This view of the Salinas Valley in California, which includes arid soils, grape crops, and vegetables, was taken with the 224-band AVIRIS sensor. This has 512 lines and 217 samples in the area covered. Similar to the IP situation, the 20 water absorption bands were deleted (in this case, bands [108-112], [154-167], and 224). For this image, all that was available was at-sensor radiance data. 16 lessons are included in SA ground truth as shown in table 4. The SA dataset is frequently employed in agricultural applications like crop classification, yield prediction, and precision farming.

Table 3: The IP Dataset's Ground Truth Classes with Their Respective Samples [45]

IP_Class_Label	IP_Class_Name	IP_No_of_Samples
C_1^{IP}	Alfalfa	46
C_2^{IP}	Corn_notill	1,428
C_3^{IP}	Corn_mintill	830
C_4^{IP}	Corn	237
C_5^{IP}	Grass_pasture	483
C_6^{IP}	Grass_trees	730
C_7^{IP}	Grass_pasture_mowed	28
C_8^{IP}	Hay_windowed	478
C_9^{IP}	Oats	20
C_{10}^{IP}	Soybean_notill	972
C_{11}^{IP}	Soybean_mintill	2,455
C_{12}^{IP}	Soybean_clean	593
C_{13}^{IP}	Wheat	205
C_{14}^{IP}	Woods	1,265
C_{15}^{IP}	Buildings_Grass_Trees_Drives	386
C_{16}^{IP}	Stone_Steel_Towers	93

Table 4: The SA Dataset's Ground Truth Classes with Their Respective Samples [45].

SA_Class_ Label	SA_Class_Name	SA_No_of_ Samples
C_1^{SA}	Brocoli_green_weeds_1	2,009
C_2^{SA}	Brocoli_green_weeds_2	3,726
C_3^{SA}	Fallow	1,976
C_4^{SA}	Fallow_rough_plow	1,394
C_5^{SA}	Fallow_smooth	2,678
C_6^{SA}	Stubble	3,959
C_7^{SA}	Celery	3,579
C_8^{SA}	Grapes_untrained	11,271
C_9^{SA}	Soil_vinyard_develop	6,203
C_{10}^{SA}	Corn_senesced_green_weeds	3,278
C_{11}^{SA}	Lettuce_romaine_4wk	1,068
C_{12}^{SA}	Lettuce_romaine_5wk	1,927
C_{13}^{SA}	Lettuce_romaine_6wk	916
C_{14}^{SA}	Lettuce_romaine_7wk	1,070
C_{15}^{SA}	Vinyard_untrained	7,268
C_{16}^{SA}	Vinyard_vertical_trellis	1,807

University of Pavia (PU) Dataset

This 610*610 pixel image was taken by the ROSIS sensor during a flight campaign over Pavia, northern Italy. Although it has 103 spectral bands, some of the samples are useless and must be removed before analysis. Geometrical resolution is 1.3 meters. The ground truth image contains nine classes (see table 5). The rejected samples appear in the figures as distant black strips. This PU dataset is frequently used for applications linked to urban remote sensing, such as anomaly detection and the classification of urban land cover.

Table 5: The PU Dataset's Ground Truth Classes with Their Respective Samples [45].

PU_Class_ Label	PU_Class_Name	PU_No_of_ Samples
C_1^{PU}	Asphalt	6,631
C_2^{PU}	Meadows	18,649
C_3^{PU}	Gravel	2,099
C_4^{PU}	Trees	3,064
C_5^{PU}	Painted_metal_sheets	1,345
C_6^{PU}	Bare_Soil	5,029
C_7^{PU}	Bitumen	1,330
C_8^{PU}	Self_Blocking_Bricks	3,682
C_9^{PU}	Shadows	947

3. EXPERIMENTS, RESULTS AND DISCUSSIONS

3.1. Experimental Setup

Building of a Discrete Wavelet 2D-CNN model for HSI classification is carried out in this paper using TensorFlow environment and Keras library packages. For patch extraction, MxMx3 is the window size. 24x24x3 is the patch size for PU and SA datasets. The patch size is set at 64x64x3 for the IP dataset. In our experiments, first, we compared the performances of various discrete mother wavelets for spectral FE in 2D-CNN-HSI classification problems. These experiments are carried out for varying number of epochs and training-testing samples. Secondly, we have provided the comparison with previous methods available for HSI classifications.

To assess the effectiveness of the framework, we selected three standard accuracy metrics: average accuracy (AA), overall accuracy (OA), and Kappa coefficient (Kappa). The OA metric calculates the ratio of correctly classified samples to the total number of test samples. The AA metric computes the average classification accuracy across different classes, while the Kappa metric quantifies the level of agreement between the classification map and the ground truth map. The momentum is established at 0.9, and the learning rate remains constant at 0.01 throughout the training process, employing the "stochastic gradient descent (SGD)" optimizer.

3.2. Classification Results
3.2.1. Comparison of HSI classification results using 2D-CNN model with various discrete mother wavelets for spectral FE

Tables 6 -11 show the classification findings, where, we conducted an accuracy assessment to investigate how different discrete mother wavelets for spectral feature extraction impact the performance of the 2D-CNN model. We compared the classification results of the CNN using three different DWT methods across different combinations of training data quantities and epochs.

From Tables 6 to 11, it's evident that across all three benchmark datasets, the CNN utilizing the D4 wavelet consistently outperforms the other configurations in terms of OA, AA, and Kappa values. Though, HAAR wavelet performs well than other wavelets on SA at 20 Epochs with constant training ratio of 10%, D4 achieves greater accuracy on the same (SA) dataset at increased number of Epochs.

Moreover, the figures from 8 to 25 depict the visualization of output maps generated by the Wavelet 2D-CNN model employing the three distinct mother wavelets across various combinations of training data ratios and epochs. It's evident that the maps utilized for visualization in cases of low categorization accuracy exhibit a coarse appearance. This is because extracting adequate and meaningful spectral-spatial aspects using the 2D-CNN model with wavelets like HAAR and CDF-9/7 poses a challenge.

Conversely, the CNN model employing the D4 wavelet managed to capture a richer set of discriminative features within the HSI data, leading to enhanced accuracy in terms of OA, AA, Kappa values, and more precise visualization maps. The total impact clearly demonstrates that the CNN model using the D4 wavelet achieves superior accuracy, highlighting the excellence of the developed method. This is attributed to the compactly supported orthogonal nature of D4, which preserves signal energy, while Haar is affected by compression through averaging and differencing. Additionally, CDF-9/7, due to its longer wavelet coefficients and scaling, necessitates more computation time compared to both D4 and Haar.

Thus, in this experiment, D4 filters outperform Haar and CDF-9/7 filters with reference to OA, AA and Kappa values, thereby provides superior categorization. Also by increasing the training ratio, the overall accuracy increased on all the datasets for D4.

3.2.2. Comparison of performance with previous models in HSI classification

To test the superiority of the strategy examined in Section 3.2.1 in terms of HSI classification accuracies, we have considered the available methods in the literature like SpectralNet [37], FuSENET [27], SSRN [40], 2D CNN [23] and 3D CNN [24].
To compute the results, we used the publicly accessible codes for the comparison models: [https://github.com/tanmayty/SpectralNET], [https://github.com/eecn/Hyperspectral-Classification].

The results of these deep learning based methods are compared with the current approach that employs 2D CNN model with Daubechies4 (D4) as its mother wavelet for spectral FE. The models have been trained for 100 epochs. The results are tested for 10% and 30% random training sets respectively. Tables 12 and 13 present the summary of investigations in terms of the OA, AA and Kappa values.

As shown in the tables 12 and 13, in both the sets, the strategy suggested in this paper for Discrete Wavelet 2D-CNN has achieved considerable success. Throughout the three datasets, the results of SSRN, FuSENET, and SpectralNET Methods appear to perform better than the results of 2D CNN and 3D CNN methods. The SpectralNET by utilizing less spectral bands performs better than the remaining models. Though it highlights the merit of using wavelets based spectral FE with a CNN, this model employs only Haar as its mother wavelet and other possible DWTs for spectral FE have not been considered. In contrast to prior models in the literature, our current study employs the lifting-scheme method to generate fully lossless DWTs for enhanced spectral FE in HSI classification. Furthermore, our present work involves verifying the performance of Discrete Wavelet 2D CNN with some more DWTs for spectral FE and comparing the results.

It can be observed from the results that the performance of Discrete Wavelet 2D CNN with D4 as mother wavelet for spectral FE is superior to all the compared methods currently available for HSI classification. Even though in the 10% train set, the SpectralNet and the SSRN models appears to perform better in terms of AA for IP and PU datasets, the proposed model with D4 wavelet is still able to outperform all the methods in remaining all cases. From the results it can be established that the performance of a basic deep learning model (such as 2D CNN) can be boosted by selecting appropriate mother wavelet for spectral FE in HSI classification.

4. CONCLUSION

The lifting-scheme based Discrete Wavelet 2D-CNN classifier for HSI is studied in this paper. To identify the optimal mother wavelet for spectral FE within this classifier, we examined and evaluated the performance of three essential discrete mother wavelets (HAAR, D4, and CDF-9/7) on three benchmark datasets (IP, PU, and SA). We assessed the classification results using metrics like OA, AA, and Kappa values.

It is discovered from the experiments that, when D4 wavelet-based FE is used, the model's accuracy is substantially higher with decent visualization maps than the accuracy gained from Haar and CDF-9/7 wavelets on the same HSI data. In addition, the results show that the performance of the Discrete Wavelet 2D CNN with D4 wavelet for spectral FE is superior to all other approaches currently in use for HSI classification. In conclusion, we observed that the wavelet-based deep learning system is particularly responsive to the choice of the mother wavelet. However, the right selection of the mother wavelet for spectral FE can lead to improved classification accuracies.

In future, the effectiveness of other varieties of mother wavelets and the improvements in accordance with the activation functions still could be tested. Further, experiments can also be made to check whether we get the same results if other deep learning classifiers are used with wavelet-based spectral FE in HSI. For example, recurrent neural networks (RNNs), and auto-encoders can be used.

Table 6: Experiment Results For Wavelet 2D-CNN With Different DWTs On IP Dataset For Various Number Of Epochs With Training Ratio Fixed At 10%

No.of Epochs	20			40			60			80		
	OA	Kappa	AA	OA	Kappa	AA	OA	Kappa	AA	OA	Kappa	AA
CNN with HAAR	92.11	91.04	79.07	96.95	96.51	91.06	97.00	96.58	91.87	97.84	97.53	94.37
CNN with D4	**95.25**	**94.58**	**80.16**	**97.49**	**97.14**	**93.47**	**97.14**	**96.74**	**92.84**	**98.17**	**97.92**	**94.38**
CNN with CDF 9/7	90.92	89.62	77.56	97.04	96.62	90.06	96.87	96.43	90.67	97.43	97.06	94.27

Table 7: Experiment Results For Wavelet 2D-CNN With Different DWTs On IP Dataset For Distinct Amounts Of Training Ratios With Epochs Fixed At 80

Training Ratio	10%			20%			30%		
	OA	Kappa	AA	OA	Kappa	AA	OA	Kappa	AA
CNN with HAAR	97.84	97.53	94.37	99.46	99.38	98.61	99.76	99.72	97.92
CNN with D4	**98.17**	**97.92**	**94.38**	**99.52**	**99.45**	**98.80**	**99.84**	**99.82**	**99.74**
CNN with CDF 9/7	97.43	97.06	94.27	98.95	98.80	98.04	99.26	99.15	98.56

Table 8: Experiment Results For Wavelet 2D-CNN With Different DWTs On SA Dataset For Various Number Of Epochs With Training Ratio Fixed At 10%

No.of Epochs	20			40			60			80		
	OA	Kappa	AA	OA	Kappa	AA	OA	Kappa	AA	OA	Kappa	AA
CNN with HAAR	**99.95**	**99.95**	**99.95**	99.95	99.94	99.94	99.97	99.96	99.96	97.53	97.26	99.23
CNN with D4	98.14	97.93	99.41	**99.96**	**99.96**	**99.96**	**99.98**	**99.97**	**99.98**	**99.94**	**99.95**	**99.94**
CNN with CDF 9/7	99.92	99.91	99.92	99.94	99.93	99.94	99.96	99.96	99.95	99.93	99.92	99.92

Table 9: Experiment Results For Wavelet 2D-CNN With Different DWTs On SA Dataset For Distinct Amounts Of Training Ratios With Epochs Fixed At 80

Training Ratio	10%			20%			30%		
	OA	Kappa	AA	OA	Kappa	AA	OA	Kappa	AA
CNN with HAAR	97.53	97.26	99.23	99.95	99.95	99.96	99.99	99.99	99.99
CNN with D4	**99.94**	**99.95**	**99.94**	**99.99**	**99.99**	**99.99**	100.0	100.0	100.0
CNN with CDF 9/7	99.93	99.92	99.92	99.99	99.99	99.98	99.97	99.97	99.99

Table 10: Experiment Results For Wavelet 2D-CNN With Different DWTs On PU Dataset For Various Number Of Epochs With Training Ratio Fixed At 10%

No.of Epochs	20			40			60			80		
	OA	Kappa	AA	OA	Kappa	AA	OA	Kappa	AA	OA	Kappa	AA
CNN with HAAR	99.24	98.99	98.15	99.63	99.51	99.02	99.35	99.14	98.84	99.64	99.52	99.15
CNN with D4	**99.26**	**99.02**	**98.46**	**99.66**	**99.55**	**99.30**	**99.52**	**99.37**	**99.15**	**99.65**	**99.54**	**99.27**
CNN with CDF 9/7	98.92	98.57	97.89	99.39	99.19	99.05	99.51	99.35	98.93	99.61	99.48	99.26

Table 11: Experiment Results For Wavelet 2D-CNN With Different DWTs On PU Dataset For Distinct Amounts Of Training Ratios With Epochs Fixed At 80

Training Ratio	10%			20%			30%		
	OA	Kappa	AA	OA	Kappa	AA	OA	Kappa	AA
CNN with HAAR	99.64	99.52	99.15	99.93	99.91	99.90	99.97	99.97	99.96
CNN with D4	**99.65**	**99.54**	**99.27**	**99.93**	**99.91**	**99.88**	**99.97**	**99.97**	**99.96**
CNN with CDF 9/7	99.45	99.32	99.11	99.92	99.90	99.86	99.94	99.95	99.94

Table 12: The Classification Accuracies (%) Using Proposed 2D-CNN With Spectral FE Based On D4 Wavelet And State-Of-The- Art Methods WITH 10% TRAINING DATA

Training Set: 10% ; No. of Epochs:100								
Methods	Dataset: IP			Dataset: PU			Dataset: SA		
	OA	Kappa	AA	OA	Kappa	AA	OA	Kappa	AA
2D CNN	80.39	78.66	68.32	96.71	95.55	94.94	96.37	95.94	94.40
3D CNN	82.60	79.85	76.50	96.33	94.91	97.09	85.10	83.30	89.66
SSRN	98.49	98.03	86.10	99.66	99.60	99.50	99.66	99.62	99.70
FuSENET	97.19	97.35	97.32	97.66	97.65	97.66	99.29	99.96	99.14
SpectralNet	98.66	98.47	98.40	99.65	99.54	99.15	99.93	99.92	99.92
This Study	98.72	98.54	97.77	99.71	99.62	99.23	99.95	99.95	99.96

Table 13: The Classification Accuracies (%) Using Proposed 2D-CNN With Spectral FE Based On D4 Wavelet And State-Of-The- Art Methods WITH 30%TRAINING DATA

Training Set: 30% ; No. of Epochs:100								
Methods	Dataset: IP			Dataset: PU			Dataset: SA		
	OA	Kappa	AA	OA	Kappa	AA	OA	Kappa	AA
2D CNN	89.20	87.50	85.98	96.50	96.58	96.10	96.95	96.91	98.47
3D CNN	90.64	89.63	91.38	97.60	96.82	97.60	94.54	94.61	97.01
SSRN	99.10	99.01	98.33	99.91	99.78	99.90	99.97	99.96	99.97
FuSENet	99.08	98.74	98.72	99.49	99.50	99.55	99.70	99.74	99.70
SpectralNET	99.76	99.72	99.40	99.97	99.96	99.96	100	100	100
This Study	99.80	99.77	99.86	99.99	99.99	99.99	100	100	100
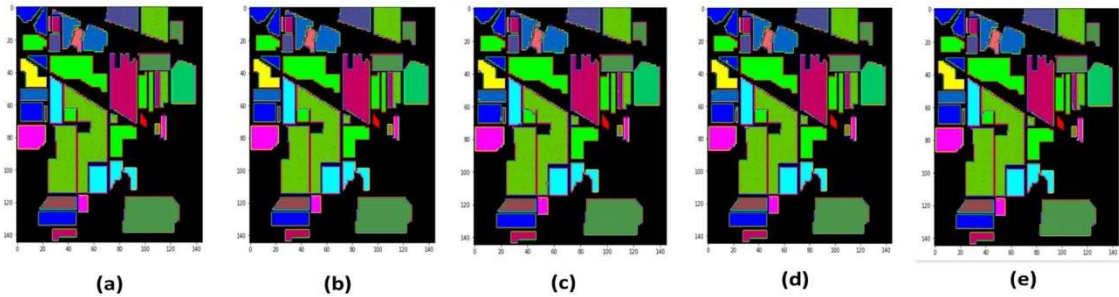
Figure 8: Visual Mapping of Indian Pines (IP) Dataset: CNN Employing the HAAR Wavelet with Varying Numbers of Epochs, and a Fixed Training Ratio of 10%. (A) Ground Truth. (B) Epochs =20 (92.11%). (C) Epochs =40 (96.95%). (D) Epochs =60 (97.00%). (E) Epochs = 80 (97.84%).
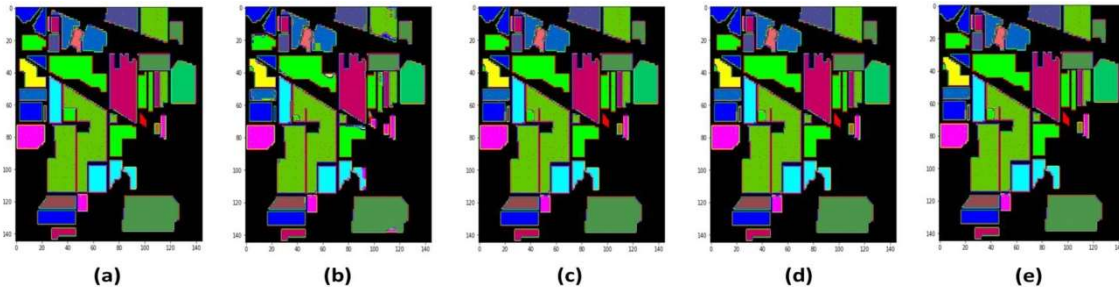
Figure 9: Visual Mapping of Indian Pines (IP) Dataset: CNN Employing the D4 Wavelet with Varying Numbers of Epochs, and a Fixed Training Ratio of 10%. (A) Ground Truth. (B) Epochs =20 (95.25%). (C) Epochs =40 (97.49%). (D) Epochs =60 (97.14%). (E) Epochs = 80 (98.17%).
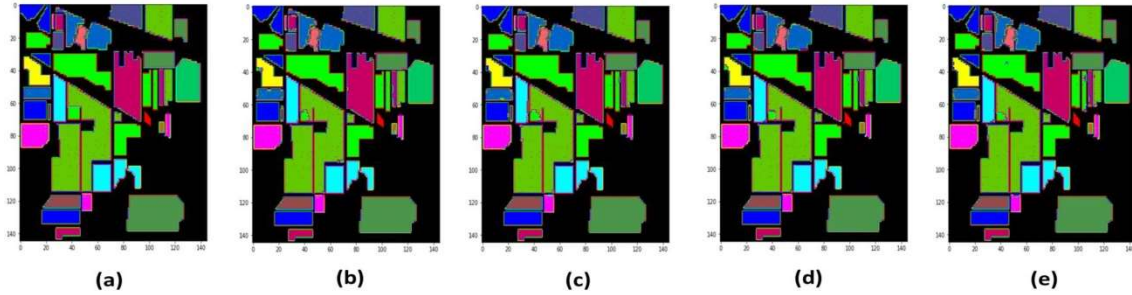
Figure 10: Visual Mapping of Indian Pines (IP) Dataset: CNN Employing the CDF-9/7 Wavelet with Varying Numbers of Epochs, and a Fixed Training Ratio of 10%. (A) Ground Truth. (B) Epochs =20 (90.92%). (C) Epochs =40 (97.04%). (D) Epochs =60 (96.87%). (E) Epochs = 80 (97.43%).
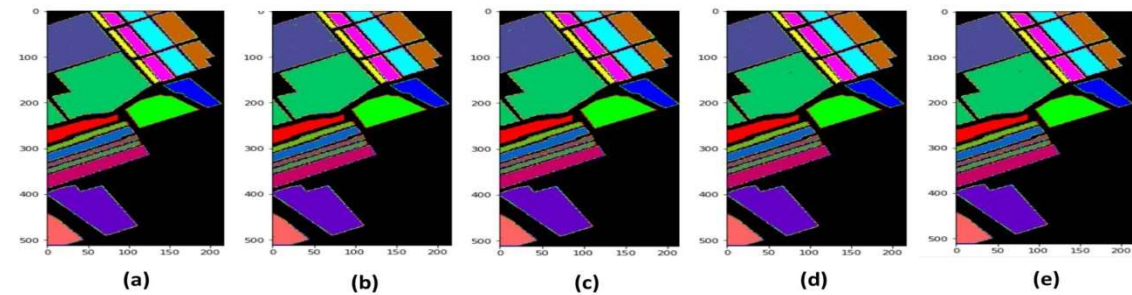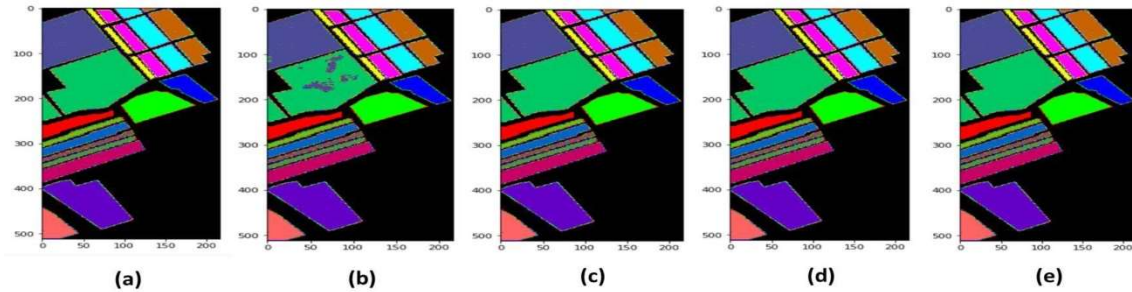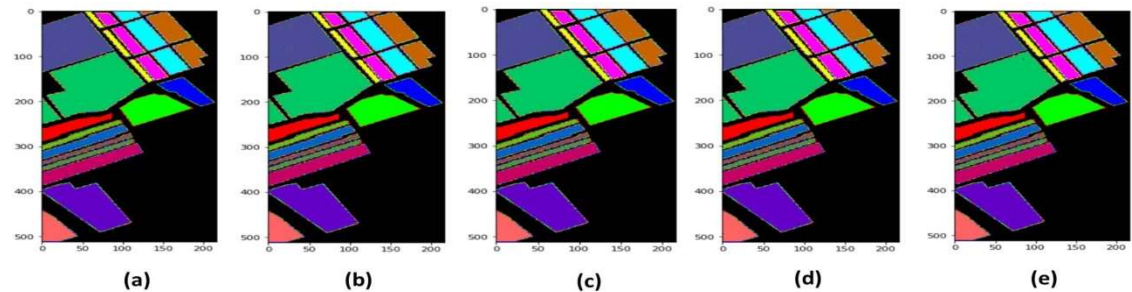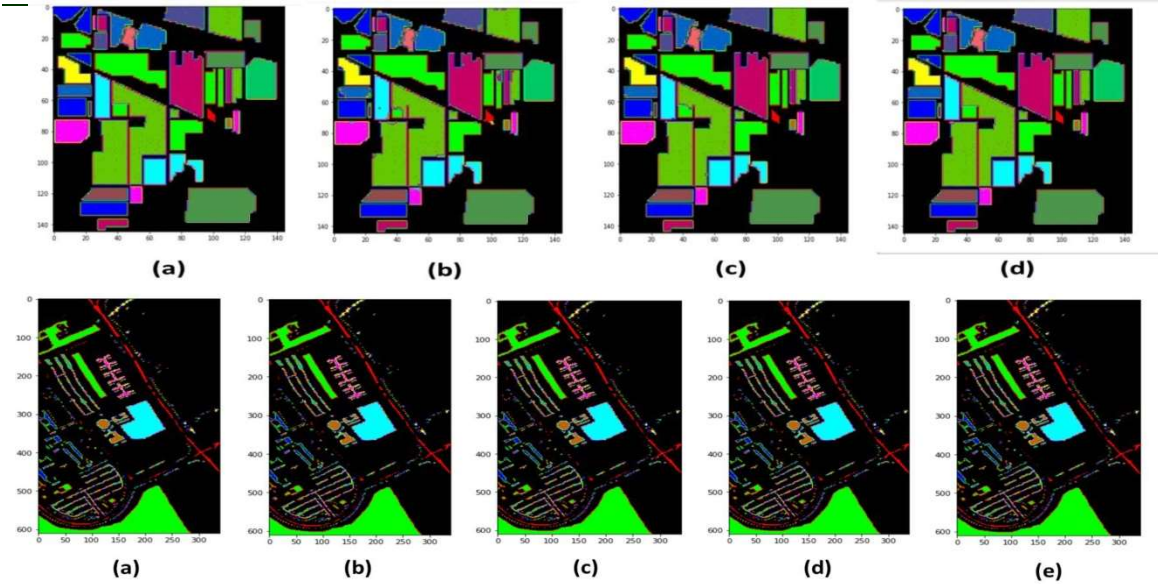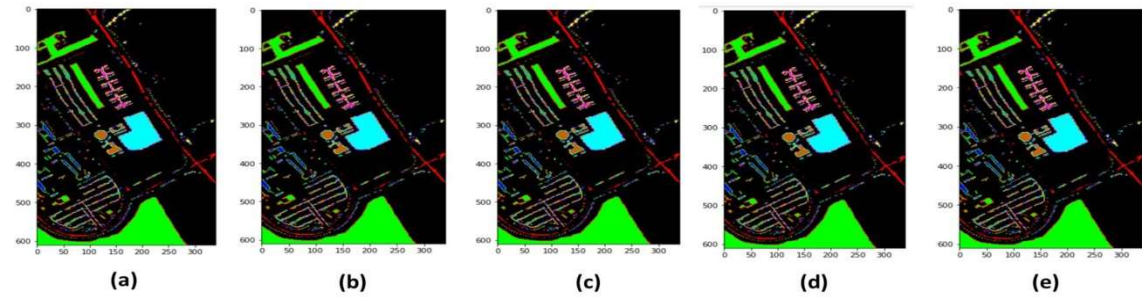

Figure 11: Visual Mapping of the Salinas (SA) Dataset: CNN Utilizing the HAAR Wavelet with Different Numbers of Epochs and a Consistent Training Ratio of 10%. (A) Ground Truth. (B) Epochs =20 (99.95%). (C) Epochs =40 (99.95%). (D) Epochs =60 (99.97%). (E) Epochs = 80 (97.53%).

Figure 12: Visual Mapping of the Salinas (SA) Dataset: CNN Utilizing the D4 Wavelet with Different Numbers of Epochs and a Consistent Training Ratio of 10%. (A) Ground Truth. (B) Epochs =20 (98.14%). (C) Epochs =40 (99.96%). (D) Epochs =60 (99.98%). (E) Epochs = 80 (99.94%).

Figure 13: Visual Mapping of the Salinas (SA) Dataset: CNN Utilizing the CDF-9/7 Wavelet with Different Numbers of Epochs and a Consistent Training Ratio of 10%. (A) Ground Truth. (B) Epochs =20 (99.92%). (C) Epochs =40 (99.94%). (D) Epochs =60 (99.96%). (E) Epochs = 80 (99.93%).

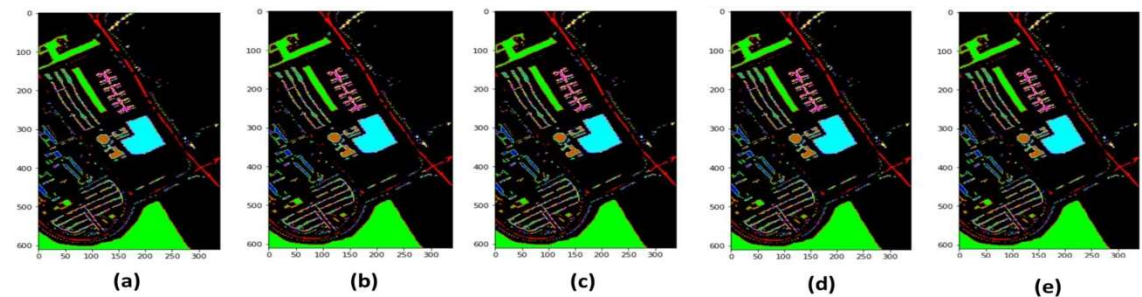*Figure 14: Visual Mapping of the University of Pavia (PU) Dataset: CNN Employing the HAAR Wavelet with Different Numbers of Epochs and a Fixed Training Ratio of 10% (A) Ground Truth. (B) Epochs =20 (99.24%). (C) Epochs =40 (99.63%). (D) Epochs =60 (99.35%). (E) Epochs = 80 (99.64%).*

Figure 15: Visual Mapping of the University of Pavia (PU) Dataset: CNN Employing the D4 Wavelet with Different Numbers of Epochs and a Fixed Training Ratio of 10% (A) Ground Truth. (B) Epochs =20 (99.26%). (C) Epochs =40 (99.66%). (D) Epochs =60 (99.52%). (E) Epochs = 80 (99.65%).

Figure 16: Visual Mapping of the University of Pavia (PU) Dataset: CNN Employing the CDF-9/7 Wavelet with Different Numbers of Epochs and a Fixed Training Ratio of 10% (A) Ground Truth. (B) Epochs =20 (98.92%). (C) Epochs =40 (99.39%). (D) Epochs =60 (99.51%). (E) Epochs = 80 (99.61%).

Figure 17: Visual Mapping of the Indian Pines (IP) Dataset: CNN Utilizing the HAAR Wavelet with Varying Training Ratios and a Fixed Number of Epochs Set at 80 (A) Ground Truth. (B) Training Ratio =10% (97.84%). (C) Training Ratio =20% (99.46 %). (D) Training Ratio =30% (99.76%).
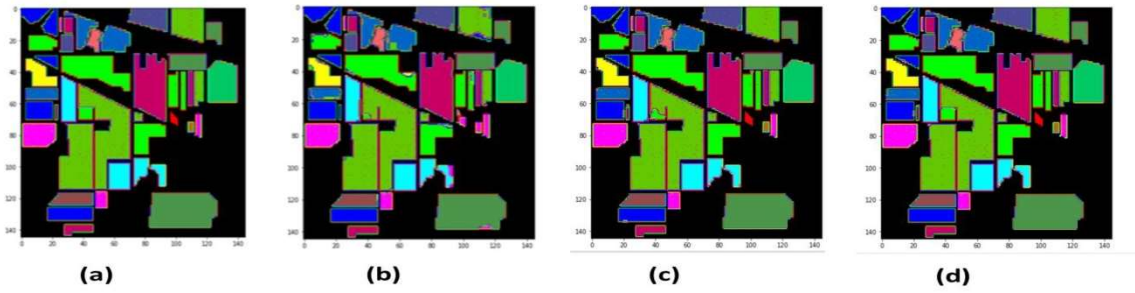
Figure 18: Visual Mapping of the Indian Pines (IP) Dataset: CNN Utilizing the D4 Wavelet with Varying Training Ratios and a Fixed Number of Epochs Set at 80 (A) Ground Truth. (B) Training Ratio =10% (98.17%). (C) Training Ratio =20% (99.52 %). (D) Training Ratio =30% (99.84%).
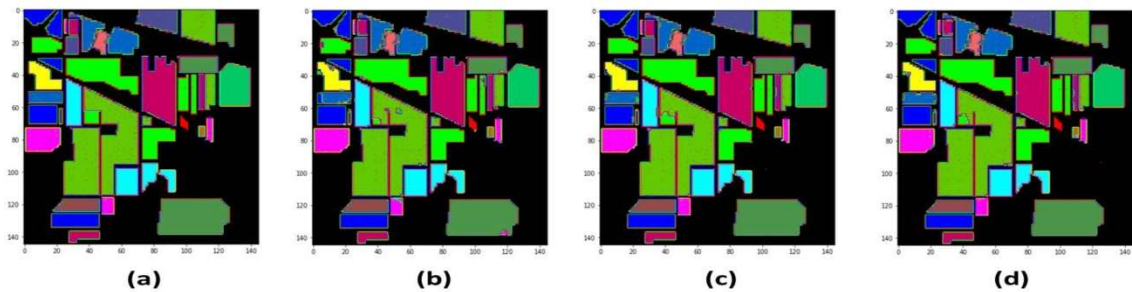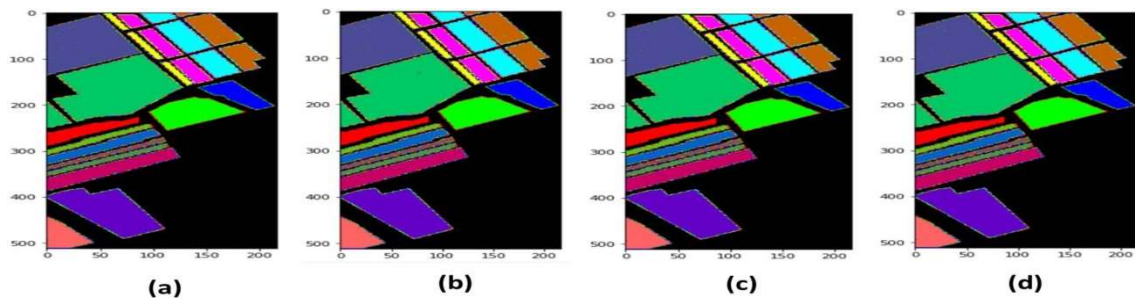

Figure 19: Visual Mapping of the Indian Pines (IP) Dataset: CNN Utilizing the CDF-9/7 Wavelet with Varying Training Ratios and a Fixed Number of Epochs Set at 80 (A) Ground Truth. (B) Training Ratio =10% (97.43%). (C) Training Ratio =20% (98.95 %). (D) Training Ratio =30% (99.26%).
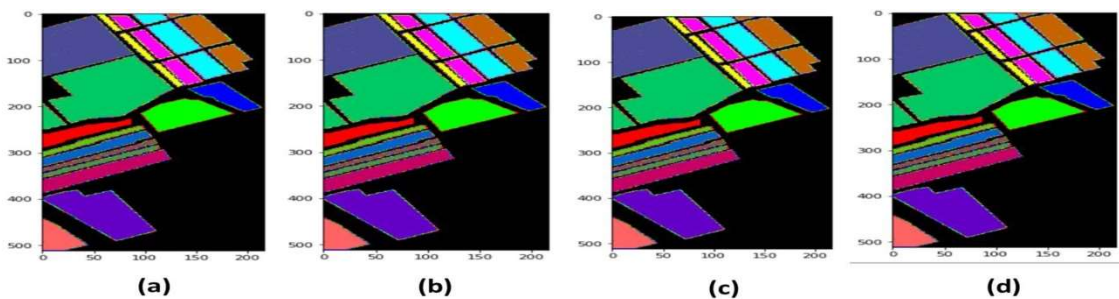

Figure 20: Visual Mapping of the Salinas (SA) Dataset: CNN Employing the HAAR Wavelet with Different Training Ratios and a Fixed Number of Epochs Set at 80 (A) Ground Truth. (B) Training Ratio =10% (97.53%). (C) Training Ratio =20% (99.95 %). (D) Training Ratio =30% (99.99%).

Figure 21: Visual Mapping of the Salinas (SA) Dataset: CNN Employing the D4 Wavelet with Different Training Ratios and a Fixed Number of Epochs Set at 80 (A) Ground Truth. (B) Training Ratio =10% (99.94%). (C) Training Ratio =20% (99.99%). (D) Training Ratio =30% (100.00%).
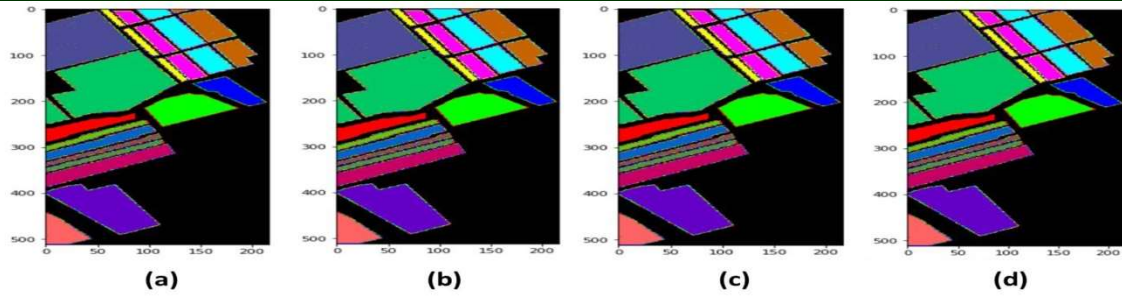
Figure 22: Visual Mapping of the Salinas (SA) Dataset: CNN Employing the CDF-9/7 Wavelet with Different Training Ratios and a Fixed Number of Epochs Set at 80 (A) Ground Truth. (B) Training Ratio =10% (99.93%). (C) Training Ratio =20% (99.99 %). (D) Training Ratio =30% (99.97%).
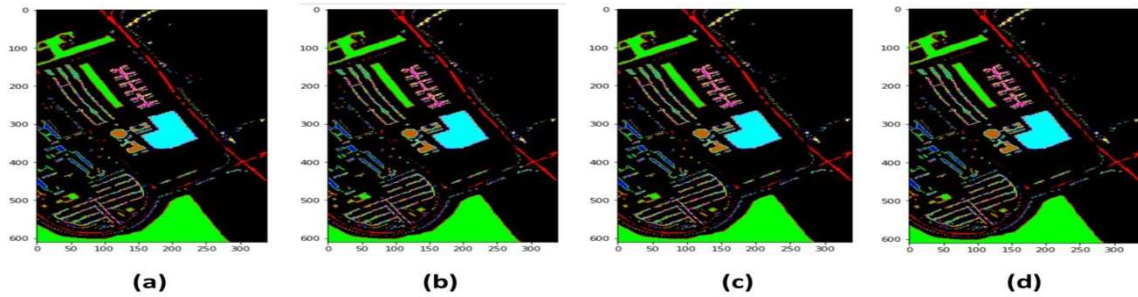

Figure 23: Visual Mapping of the University of Pavia (PU) Dataset: CNN Utilizing the HAAR Wavelet with Different Training Ratios and a Fixed Number of Epochs Set at 80 (A) Ground Truth. (B) Training Ratio =10% (99.64%). (C) Training Ratio =20% (99.93 %).(D) Training Ratio =30% (99.97%).
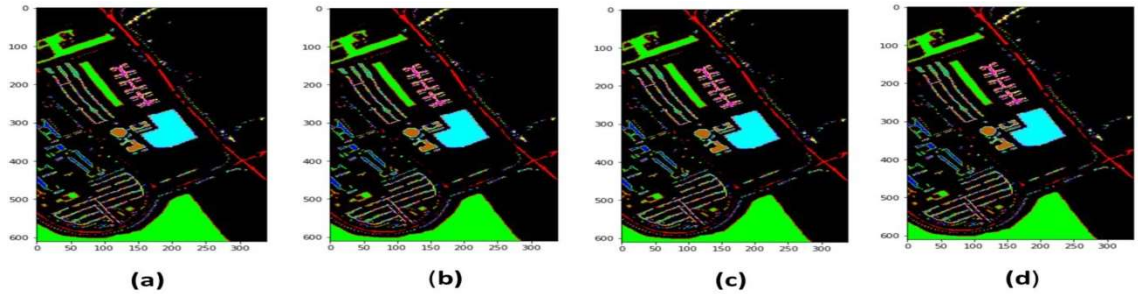

Figure 24: Visual Mapping of the University of Pavia (PU) Dataset: CNN Utilizing the D4 Wavelet with Different Training Ratios and a Fixed Number of Epochs Set at 80 (A) Ground Truth. (B) Training Ratio =10% (99.65%). (C) Training Ratio =20% (99.93 %). (D) Training Ratio =30% (99.97%).
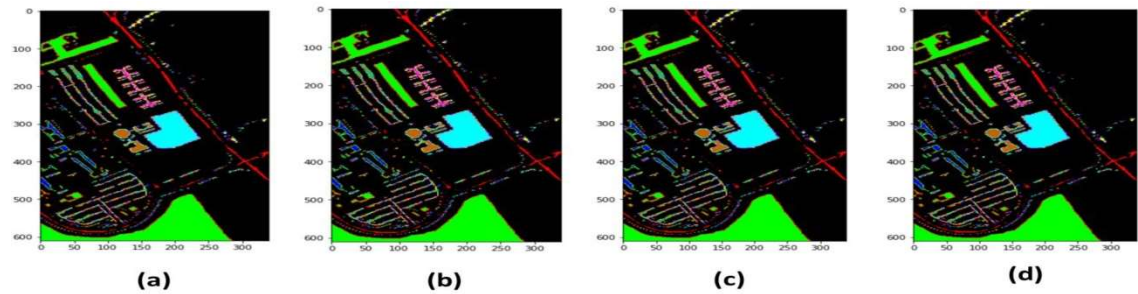

Figure 25: Visual Mapping of the University of Pavia (PU) Dataset: CNN Utilizing the CDF-9/7 Wavelet with Different Training Ratios and a Fixed Number of Epochs Set at 80 (A) Ground Truth. (B) Training Ratio =10% (99.45%). (C) Training Ratio =20% (99.92 %). (D) Training Ratio =30% (99.94%).

REFERENCES:

[1] Q.Zhu , W.Deng , Z.Zheng ,Y.Zhong , Q.Guan , W.Lin, L.Zhang , and D.Li, "A Spectral-Spatial-Dependent Global Learning Framework for Insufficient and Imbalanced Hyperspectral Image Classification", IEEE Transactions on Cybernetics, Vol.52, No.11, Pp.11709-11723, Doi: 10.1109/Tcyb.2021.3070577.

[2] M.E. Paoletti, J.M. Haut, J. Plaza, And A. Plaza, "Deep Learning Classifiers for Hyperspectral Imaging: A Review", ISPRS Journal of Photogrammetry and Remote Sensing 158 (2019) 279-317.

[3] Shrutika Sawant, Prabukumar Manoharan, "Hyperspectral band selection based on metaheuristic optimization approach," Infrared Physics & Technology, Volume 107, 2020, 103295, ISSN 1350-4495.

[4] Musa Peker, "Classification of hyperspectral imagery using a fully complex-valued wavelet neural network with deep convolutional features", Expert Systems With Applications 173 (2021) 114708.

[5] S. Li, W. Song, L. Fang, Y. Chen, P. Ghamisi, and J. A. Benediktsson, "Deep learning for hyperspectral image classification: An overview," IEEE Transactions on Geoscience and Remote Sensing, vol. 57, no. 9, pp. 6690–6709, 2019.

[6] T. Lu, S. Li, L. Fang, X. Jia, and J. A. Benediktsson, "From subpixel to superpixel: A novel fusion framework for hyperspectral image classification," IEEE Trans. Geosci. Remote Sens., vol. 55, no. 8, pp. 4398–4411, Aug. 2017.

[7] S. Jia, L. Shen, J. Zhu, and Q. Li, "A 3-D gabor phase-based coding and matching framework for hyperspectral imagery classification," IEEE Trans. Cybern., vol. 48, no. 4, pp. 1176–1188, Apr. 2018.

[8] G. Camps-Valls, L. Gomez-Chova, J. Muñoz-Marı, J. Vila-Francés, and J. Calpe-Maravilla, "Composite kernels for hyperspectral image classification," IEEE Trans. Geosci. Remote Lett., vol. 3, no. 1, pp. 93–97,Jan. 2006.

[9] L. Fang, S. Li, W. Duan, J. Ren, and J. A. Benediktsson, "Classification of hyperspectral images by exploiting spectral–spatial information of superpixel via multiple kernels," IEEE Trans. Geosci. Remote Sens., vol. 53, no. 12, pp. 6663–6674, Dec. 2015.

[10] L. Fang, N. He, S. Li, P. Ghamisi, and J. A. Benediktsson, "Extinction profiles fusion for hyperspectral images classification," IEEE Trans.Geosci. Remote Sens., vol. 56, no. 3, pp. 1803–1815, Mar. 2018.

[11] Shambulinga M, G. Sadashivappa, "Hyperspectral Image Classification using Convolutional Neural Networks," (IJACSA) International Journal of Advanced Computer Science and Applications,Vol. 12, No. 6, 2021.

[12] T. N. Prabhakar and P. Geetha, "Two-dimensional empirical wavelet transform based supervised hyperspectral image classification," ISPRS Journal of Photogrammetry and Remote Sensing, vol. 133, pp. 37 – 45, 2017.

[13] Mallat, S.G., "A theory for multi resolution signal decomposition: the wavelet representation", IEEE transactions on Pattern Analysis and Machine Intelligence, 11(7), pp. 674-693, 1989.

[14] R. Anand S.Veni and J. Aravinth, "Robust Classification Technique for Hyperspectral Images Based on 3d-Discrete Wavelet Transform", Remote Sens. 2021, 13, 1255. https://doi.org/10.3390/rs13071255

[15] Chilo J, Lindblad T. Hardware implementation of 1D wavelet transform on an FPGA for infrasound signal classification. Nuclear Science. IEEE Transactions. 2008 Feb; 55(1):9–13.

[16] Acharya T, Chakrabarti C. A survey on lifting-based discrete wavelet transform architectures. Journal of VLSI Signal Processing Systems for Signal, Image and Video Technology. 2006 Mar; 42(3):321–39.

[17] Andra K, Chakrabarti C, Acharya T. A VLSI architecture for lifting-based forward and inverse wavelet transform. Signal Processing, IEEE Transactions. 2002 Apr; 50(4):966–77.

[18] Lan X, Zheng N, Liu Y. Low-power and high-speed VLSI architecture for lifting-based forward and inverse wavelet transform. Consumer Electronics. IEEE Transactions. 2005 May; 51(2):379–85.

[19] Liao H, Mandal MK, Cockburn BF. Efficient architectures for 1-D and 2-D lifting-based wavelet transforms. Signal Processing, IEEE Transactions. 2004 May; 52(5):1315–26.

[20] Mahmoud MI, Dessouky MIM, Deyab S, Elfouly FH. Comparison between Haar and Daubechies wavelet transformations on FPGA technology. International Journal of Electrical, Computer, Electronics and Communication Engineering. World Academy of Science, Engineering and Technology. 2008; 2(1):133–7.

[21] Pang J, Chauhan S, Bhalodia JM. Speech Compression FPGA Design By Using Different Discrete Wavelet Transform Schemes.

Advances in Electrical and Electronics Engineering and Computer Science. World Congress on Engineering and Computer Science. San Francisco, CA. 2008 Oct 22-24; 21–9.

[22] W.Guo, G.Xu, B.Liu and Y.Wang, "Hyperspectral Image Classification Using CNN-Enhanced Multi-Level Haar Wavelet Features Fusion Network," IEEE GEOSCIENCE AND REMOTE SENSING LETTERS, VOL. 19, 2022.

[23] K. Makantasis, K. Karantzalos, A. Doulamis, and N. Doulamis, "Deep Supervised Learning for Hyperspectral Data Classification Through Convolutional Neural Networks," In Ieee International Geoscience and Remote Sensing Symposium (Igarss). Ieee, 2015, Pp. 4959–4962.

[24] Ben Hamida, A. Benoit, P. Lambert, and C. Ben Amar, "3-D Deep Learning Approach for Remote Sensing Image Classification," IEEE Transactions on Geoscience and Remote Sensing, vol. 56, no. 8, pp. 4420–4434,2018.

[25] X. Yang, Y. Ye, X. Li, R. Y. K. Lau, X. Zhang, and X. Huang, "Hyperspectral image classification with deep learning models," IEEE Transactions on Geoscience and Remote Sensing, vol. 56, no. 9, pp. 5408–5423, 2018.

[26] M. Han, R. Cong, X. Li, H. Fu, and J. Lei, "Joint spatial-spectral hyperspectral image classification based on convolutional neural network," Pattern Recognition Letters, vol. 130, pp. 38 – 45, 2020. Image/Video Understanding and Analysis (IUVA).

[27] S. K. Roy, "Fusenet: fused squeeze-and-excitation network for spectral-spatial hyperspectral image classification," IET Image Processing, vol. 14, pp. 1653–1661(8), June 2020.

[28] J. Zheng, Y. Feng, C. Bai, and J. Zhang, "Hyperspectral image classification using mixed convolutions and covariance pooling," IEEE Transactions on Geoscience and Remote Sensing, pp. 1–13, 2020.

[29] Z. Ge, G. Cao, X. Li, and P. Fu, "Hyperspectral image classification method based on 2d–3d cnn and multibranch feature fusion," IEEE Journal of Selected Topics in Applied Earth Observations and Remote Sensing, vol. 13, pp. 5776–5788, 2020.

[30] W. Song, S. Li, L. Fang, and T. Lu, "Hyperspectral image classification with deep feature fusion network," IEEE Trans. Geosci. Remote Sens., vol. 56, no. 6, pp. 3173–3184, Jun. 2018.

[31] L. Mou, P. Ghamisi, and X. X. Zhu, "Deep recurrent neural networks for hyperspectral image classification," IEEE Trans. Geosci. Remote Sens., vol. 55, no. 7, pp. 3639–3655, Jul. 2017.

[32] H. Wu and S. Prasad, "Convolutional recurrent neural networks for hyperspectral data classification," Remote Sens., vol. 9, no. 3, p. 298, Mar. 2017.

[33] Z. Feng, S. Yang, M. Wang, and L. Jiao, "Learning dual geometric low-rank structure for semisupervised hyperspectral image classification," IEEE Trans. Cybern., vol. 51, no. 1, pp. 346–358, Jan. 2021.

[34] Z. Zhong, J. Li, D. A. Clausi, and A. Wong, "Generative adversarial networks and conditional random fields for hyperspectral image classification," IEEE Trans. Cybern., vol. 50, no. 7, pp. 3318–3329, Jul. 2020.

[35] S. K. Roy, G. Krishna, S. R. Dubey, and B. B. Chaudhuri, "Hybridsn: Exploring 3-d–2-d cnn feature hierarchy for hyperspectral image classification," IEEE Geoscience and Remote Sensing Letters, vol. 17, no. 2, pp. 277–281, 2020.

[36] L. Mou, X. Lu, X. Li, and X. X. Zhu, "Nonlocal graph convolutional networks for hyperspectral image classification," IEEE Transactions on Geoscience and Remote Sensing, vol. 58, pp. 1–12, 2020.

[37] T. Chakraborty and U. Trehan, "SpectralNET: Exploring spatial–spectral WaveletCNN for hyperspectral image classification," 2021, arXiv:2104.00341.

[38] W. Guo, G. Xu, W. Liu, B. Liu, and Y. Wang, "CNN-combined graph residual network with multilevel feature fusion for hyperspectral image classification," IET Comput. Vis., vol. 15, no. 8, pp. 592–607, Dec. 2021.

[39] Z. Zheng, Y. Zhong, A. Ma, and L. Zhang, "FPGA: Fast patch-free global learning framework for fully end-to-end hyperspectral image classification," IEEE Trans. Geosci. Remote Sens., vol. 58, no. 8, pp. 5612–5626, Aug. 2020.

[40] Z. Zhong, J. Li, Z. Luo, and M. Chapman, "Spectral–spatial residual network for hyperspectral image classification: A 3-d deep learning framework," IEEE Transactions on Geoscience and Remote Sensing, vol. 56, no. 2, pp. 847–858, 2018.

[41] P. Liu, H. Zhang, W. Lian, and W. Zuo, "Multi-Level Wavelet Convolutional Neural Networks," IEEE Access, vol. 7, pp. 74973-74985, 2019.

[42] Chu He, Z.Shi, T.Qu, D. Wang and M. Liao, "Lifting Scheme-Based Deep Neural Network for Remote Sensing Scene Classification," Remote Sens. 2019, 11, 2648; doi:10.3390/rs11222648.

[43] P.H. AnilKumar and P.A.S. Beulet, "Lifting-based Discrete Wavelet Transform for Real-Time Signal Detection," Indian Journal of Science and Technology, Vol 8(25), DOI: 10.17485/ijst/2015/v8i25/80301, October 2015.

[44] Daubechies I, Sweldens W. Factoring wavelet transform into lifting steps. Journal of Fourier analysis and Applications. 1998 May; 4(3):247–69.

[45] Grupo de Inteligencia Computacional (GIC). (2021). Hyper spectral Remote Sensing Scenes [Online].Available at: https:// www.ehu.eus/ ccwintco/index.php/Hyperspectral_Remote_Sensing_Scenes# Indian_Pines (Accessed: 14 Oct 2022).